J. Fluid Mech. (2002), *vol.* 457, *pp.* 133–156. © 2002 Cambridge University Press
DOI: 10.1017/S0022112001007637 Printed in the United Kingdom

Experiments on laminar film flow along a periodic wall

By M. VLACHOGIANNIS AND V. BONTOZOGLOU

Department of Mechanical and Industrial Engineering, University of Thessaly, GR-38334 Volos, Greece

(Received 1 December 2000 and in revised form 18 June 2001)

Experimental results are reported on the structure of gravity-driven film flow along an inclined periodic wall with rectangular corrugations. A fluorescence imaging method is used to capture the evolution of film height in space and time with accuracy of a few microns. The steady flow is found to exhibit a statically deformed free surface, as predicted by previous asymptotic and numerical studies. Though usually unstable, its characteristics determine much of the subsequent non-stationary dynamics. Travelling disturbances are observed to evolve into solitary multi-peaked humps, and pronounced differences from the respective phenomena along a flat wall are noted. Finally, a remarkable stabilization of the flow at high Reynolds numbers is documented, which proceeds through the development of a three-dimensional flow structure and leads to a temporary decrease in film thickness and recession of solitary waves.

1. Introduction

The flow of a liquid film along a wavy – rather than flat – wall is an interesting variation of the fundamental fluid mechanics problem of gravity-driven film flow. It has various engineering applications, related to interfacial and wall transfer rate control by disturbing the basic flow field through wall corrugations. Examples are found in the proprietary designs of surfaces of two-phase heat exchangers (Focke & Knibbe 1986; Shah & Focke 1988; Webb 1994) and in the various shapes of structured packings, used to improve gas–liquid contact in absorption columns and distillation trays (Fair & Bravo 1990; deSantos, Melli & Scriven 1991).

Despite numerous applications, the fundamental problem seems to have motivated relatively little theoretical and experimental work. Papers referring to film flow over a wall that is not flat include Wang (1981), who performed an asymptotic analysis for a sinusoidal wall with small-amplitude variations, and Dassori, Deiber & Cassano (1984) and Kang & Chen (1995), who extended the analysis to the separated flow of two fluids. Also, Pozrikidis (1988) used a boundary-integral method and numerically computed results for wall variations of arbitrary amplitude and shape, and Shetty & Cerro (1993) proved by asymptotic analysis that, in the limit of negligible inertia and capillary effects, the flow of a viscous liquid down a wavy surface obeys a local Nusselt solution. The aforementioned works are applicable to flow with Reynolds number very close to zero. Note also that some of the above papers refer to vertical walls with large-amplitude corrugations. The resulting ratio of film thickness to wall amplitude is roughly an order of magnitude smaller than in the present work, which involves slightly inclined films over smaller disturbances. This could cast some doubt on the direct relevance of these papers to the present experiment.

Recently, Bontozoglou & Papapolymerou (1997) studied film flow at finite Reynolds number in the linear limit of small-amplitude, sinusoidal corrugations. They calculated a weak resonant interaction for $Re = O(10^2)$ resulting in a static deformation of the free surface with amplitude up to twice that of the wall. The wavelength of the corrugations resulting in maximum amplification was reported in the range 10^{-3}–10^{-2} m and was predicted to vary with wall inclination.

Numerical computations for two-dimensional, steady flow along large-amplitude corrugations were performed for a limited range of the parameter space by Trifonov (1998*a*), Malamataris & Bontozoglou (1999) and Bontozoglou (2000). The computations confirmed that there is a change in the flow structure around the resonant conditions of linear theory, manifested by an increase of the free surface deformation and a recession of the separation bubble inside the corrugation troughs.

All the aforementioned computational and asymptotic predictions are restricted to steady flow, being the equivalent of the Nusselt solution for a flat wall. In particular, there are no predictions available concerning the occurrence and properties of time-varying flows, such as progressive waves. Experimental information on the problem is even more limited; the only data in the literature are by Zhao & Cerro (1992) and Shetty & Cerro (1993) for very small Reynolds numbers and there is no experimental information at all for $Re > 10$.

In the present work, we apply a fluorescence imaging method in order to document the evolution in space and time of a film down an inclined wall with periodic corrugations. The main motivation is to test the computational and asymptotic predictions of steady flow and to investigate possible unsteady flow regimes. We cover the range of small inclination angles ($1^\circ < \varphi < 8^\circ$) and intermediate-to-high Reynolds numbers ($10 < Re < 400$).

2. Experimental method

In this section, the flow loop and measuring system are described. Emphasis is placed on the elements of the fluorescence technique and image analysis that are special to the present problem of film flow along a corrugated wall. Further details of the experimental setup may be found in a previous paper (Vlachogiannis & Bontozoglou 2001).

2.1. *Experimental apparatus*

The experimental apparatus, shown schematically in figure 1, consists of four major components: the overflow tank which provides a constant head; the main channel, which is 800 mm long by 250 mm wide by 20 mm high; the removable part of the channel bottom (500 mm by 250 mm), which can accommodate flat or corrugated walls; and the computer-based image grabbing and analysis system. Observations are assisted by the use of a RedLake® Motion Scope PCI high-speed video camera, with maximum speed of 1000 frames/second.

The main channel is made of plexiglas, and the entire apparatus is massive and mounted on rubber sheet to reduce the influence of vibrations (peripheral components are also connected to the main channel by flexible hoses). The geometry of the corrugated wall used in the present experiments is shown in figure 2. It consists of a square wave with wavelength $L = 12$ mm (split into 6 mm of elevation and 6 mm of depression) and height $2b = 0.4$ mm. The removable plate whose upper surface constitutes the corrugated wall is also made of plexiglas, and has been shaped with a CNC milling machine with tolerance of 6 μm.

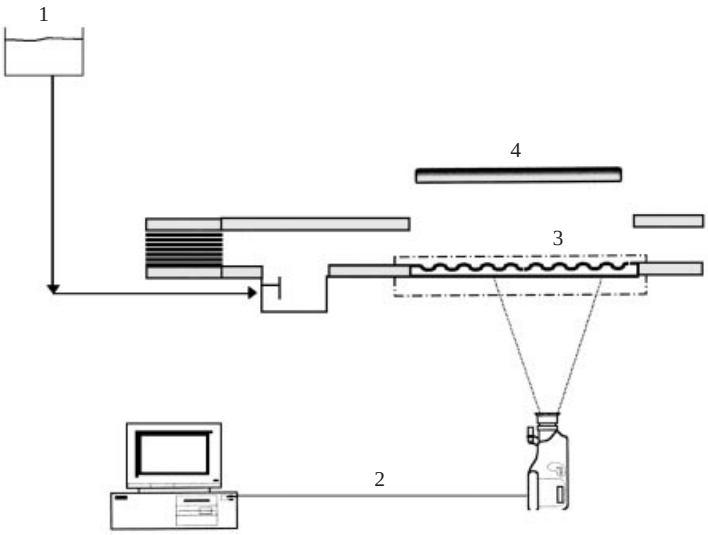

FIGURE 1. Sketch of the experimental apparatus: 1, overflow tank; 2, image grabbing system; 3, corrugated wall; 4, UV light source.

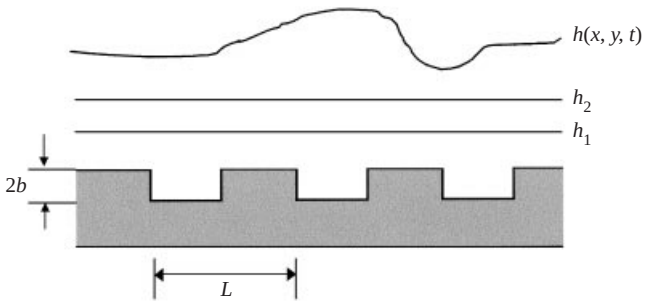

FIGURE 2. The characteristic dimensions of the corrugated wall and a graphical representation of the calibration procedure used in the experiments.

The selection of the specific wall geometry was motivated by two considerations. First, a wall consisting of horizontal and vertical sections permits application of the fluorescence imaging method with a minimum of corrections, whereas a wall with continuously varying slope (such as a sinusoidal wall) distorts the intensity image because of refraction caused by the non-zero incidence angle of the light on the interface of the two media (plexiglas and water) with different optical properties. Second, a square wave may be considered as a Fourier series of harmonics of the fundamental wavelength. Consequently, the results may provide information on the role of multiple superharmonics on the film flow.

The liquids used in the experiments are pure water and 26% by weight solution of glycerol in water. The experiments with the water–glycerol solution are performed at a temperature of 25 °C. Thus, kinematic viscosity $\nu = 2.136 \times 10^{-6}\,\mathrm{m^2\,s^{-1}}$ and surface tension $\sigma = 70 \pm 1 \times 10^{-3}\,\mathrm{N\,m^{-1}}$. The Kapitza number,

$$Ka = \sigma/\rho g^{1/3}\nu^{4/3}, \tag{1}$$

which characterizes the liquid is $Ka = 3365$ for water and $Ka = 1102$ for the

water–glycerol solution. The Reynolds number is defined as

$$Re = q/\nu = \langle u \rangle h_N/\nu \tag{2}$$

where q is the volumetric flow rate per unit width, h_N is the Nusselt film thickness and $\langle u \rangle$ is the average streamwise velocity. The flow is also characterized by the Weber number, defined as

$$We = \sigma/\rho\langle u \rangle^2 h_N. \tag{3}$$

We is not independent, but is related to Ka, Re and inclination angle, φ, through the expression

$$We = \left(\frac{3}{\sin\varphi}\right)^{1/3} \frac{Ka}{Re^{5/3}}. \tag{4}$$

2.2. *Implementation of the fluorescence imaging method*

To record the spatio-temporal variation of the film thickness over the corrugated wall, we use the fluorescence imaging method. The method has been developed by Liu, Paul & Gollub (1993), and its implementation in the present channel with a flat wall was described in a previous paper (Vlachogiannis & Bontozoglou 2001). By doping the fluid with a small concentration of dye (200–300 p.p.m. of sodium salt of fluorescein-$C_{20}H_{10}O_5Na_2$), the film fluoresces under ultraviolet illumination. A shuttered high-resolution CCD camera and a monochrome frame grabber board are used to acquire and digitize the images (576×768 pixels with 8-bit of resolution).

For relatively thin films ($h < 1.5$ mm), the fluorescence intensity $I(x, y, t)$ is satisfactorily represented as a linear function of the local film thickness $h(x, y, z)$. Thus

$$I(x, y, t) = a(x, y)h(x, y, t) + b(x, y). \tag{5}$$

Here, $a(x, y)$ and $b(x, y)$ are the two linear coefficients, which depend on the concentration of dye, the solution, the surface roughness of the wall plate and the distance and distribution of the ultraviolet source. To increase the accuracy of the data, independent a and b values are used for each pixel of the digitized image.

The calibration procedure for film flow along the corrugated wall must overcome the following difficulties. First, above the troughs of the corrugation, the film thickness is occasionally at the limit of applicability of the linear approximation, equation (5). The situation is depicted in figure 3, where the light-intensity versus liquid-height data over a thickness range of 2 mm are satisfactorily fitted only by a quadratic correlation. A second difficulty is that the surface treatment of the wall troughs (produced by the milling process) differs somewhat from that of the crests, which consist of the original plate surface. Thus, light is scattered to a different extent from the two places, and there is a step change in the values of the linear coefficient $a(x, y)$ of equation (5).

The calibration procedure adopted to overcome the above difficulties is demonstrated schematically in figure 2. It is based on the observation (to be elaborated in § 5) that, at small inclination angles and Reynolds numbers $Re \sim O(10^0$–$10^1)$, the stable film has a flat free surface. Light intensity measurements are taken in this stable range, and the prevailing uniform film thickness is measured independently by a displacement micrometer. The data, $I_1(x, y)$ and h_1, corresponding to the smallest Reynolds number used, Re_1, are considered as the baseline. The rest of the calibration measurements serve to determine the coefficient $a(x, y)$ from a linear fit of the data by the expression

$$I_2(x, y) - I_1(x, y) = a(x, y)(h_2 - h_1). \tag{6}$$

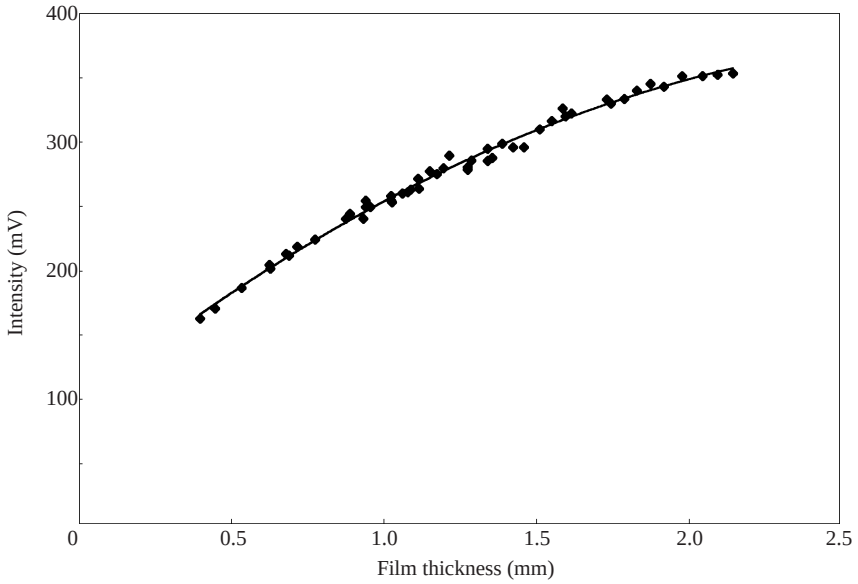

FIGURE 3. The digitized fluorescence intensity plotted as a function of liquid film thickness for 26% wt. water–glycerol solution: ◆, data for a specific pixel of the digitized image; ——, quadratic fit of the data.

Then, the instantaneous value of the film thickness in an experimental run is determined from the expression

$$h(x, y, t) = \frac{I(x, y, t) - I_1(x, y)}{a(x, y)} + h_1. \tag{7}$$

Using the above calibration, any inhomogeneities in the light scattering properties of the surface are eliminated. Furthermore, the relation between film height and light intensity is essentially linearized around the minimum height, h_1, instead of around $h = 0$. In this way, the linear relation (7) is found to represent satisfactorily all the data. An additional benefit of the procedure is that the elevation of the free surface – rather than the film thickness – is what is obtained, since the additional light intensity generated by the fluid inside the troughs is automatically taken into account.

2.3. *Data presentation and analysis*

The raw data consist of instantaneous images of a view window with dimensions 80 mm × 110 mm. When the flow is two-dimensional, the usual form of presentation involves line profiles of the free surface taken in the streamwise direction and at the centreplane of the channel. When three-dimensional phenomena occur, they are presented by iso-elevation contours of the entire image. To minimize the effect of digitization noise, the raw data are first smoothed by an appropriate convolution filter (Gaussian 7X7). An alternative procedure is to take the desired line profile first and then fit it with a high-order polynomial. However, the latter procedure occasionally fails to represent faithfully the high-harmonic content of the data and was abandoned.

Some of the results to follow are derived by Fourier decomposing the original data. More precisely, we compute the one-dimensional spatial Fourier transform of the instantaneous free surface profile. For a length-N input vector $h(x_0 + n\Delta x, y_0, t_0)$, $n = 1, \ldots N$ (consisting of the free surface elevation at each pixel of the scanned line $y = y_0$ at time $t = t_0$) we produce the length-N vector $H(k, y_0, t_0)$ by the discrete

formula

$$H(k, y_0, t_0) = \sum_{n=1}^{N} h(x_0 + n\Delta x, y_0, t_0) \exp\left(-\mathrm{i}2\pi(k-1)\frac{n-1}{N}\right), \quad 1 \leqslant k \leqslant N \qquad (8)$$

The range of wavenumbers faithfully represented is limited by the length of the window of view, 85 mm or 114 mm, and by the available spatial discretization, $\Delta x = 0.13$ mm. In some cases, the variation with time of the amplitude $H(k, y_0, t_0)$ of the kth spatial harmonic is examined by subsequently taking its temporal Fourier transform. Here, accuracy is more drastically limited by the data collection frequency, 20 Hz. When the free surface elevation time-series $h(x_0, y_0, t_0 + n\Delta t)$ at a fixed location (x_0, y_0) of the channel is used as the input vector, equation (8) also produces the temporal Fourier transform.

3. Stability of film flow along a periodic wall

Above a certain Reynolds number, dependent on the inclination angle φ, falling film flow becomes linearly unstable. For flow along a flat inclined wall, the instability is known to be of the long-wave variety with critical Reynolds number $Re_c = (5/6)\cot\varphi$ (Benjamin 1957; Yih 1963). This result has been confirmed experimentally by the detailed measurements of Liu *et al.* (1993). As a first step in the present study of film flow along a wall with periodic corrugations, we observe the conditions under which the free surface first becomes unstable. Our results are valid only for the specific wall considered, and no attempt was made to investigate the effect of corrugation size and shape.

The base flow will be considered in more detail later. It will be shown in particular that, for $Re \sim O(10^0\text{–}10^1)$ the free surface is practically flat, whereas for $Re \sim O(10^2)$, it is significantly deformed. The method used to test the stability of this base flow is to introduce a localized disturbance with a wide frequency spectrum at the inlet and observe its evolution downstream. With increasing Reynolds number, there is a well-characterized transition from a uniform (and fast) decay of all harmonics to the growth and sustenance of a series of long waves. Measurements of the critical Reynolds number for both pure water and 26% glycerol-in-water solutions are shown as points in figure 4. The two series of data fall on the same curve, confirming that the instability is still a long-wave one, characterized only by Re and not by Ka.

Also shown as a solid line in figure 4 is the theoretical prediction $Re_c = (5/6)\cot\varphi$, for a flat wall. According to the present data, the wall corrugations broaden the range of stable values of Reynolds number by roughly 30%. Thus, they have a stabilizing effect on film flow. This result is in agreement with computational predictions by Trifonov (1998*b*), who used Floquet theory to show that a film falling along a vertical periodic wall becomes linearly unstable only above a finite (though generally small) Reynolds number.

4. Outline of observed flow regimes

A variety of flows is observed in the present experiments, over the range of Reynolds numbers $10 < Re < 400$ and inclination angles $1^\circ < \varphi < 8^\circ$. The information is categorized into a number of flow regimes, and the rest of the paper is devoted to their documentation and the analysis of their properties. To facilitate the reader, an outline of the main features of each flow regime is provided at this point.

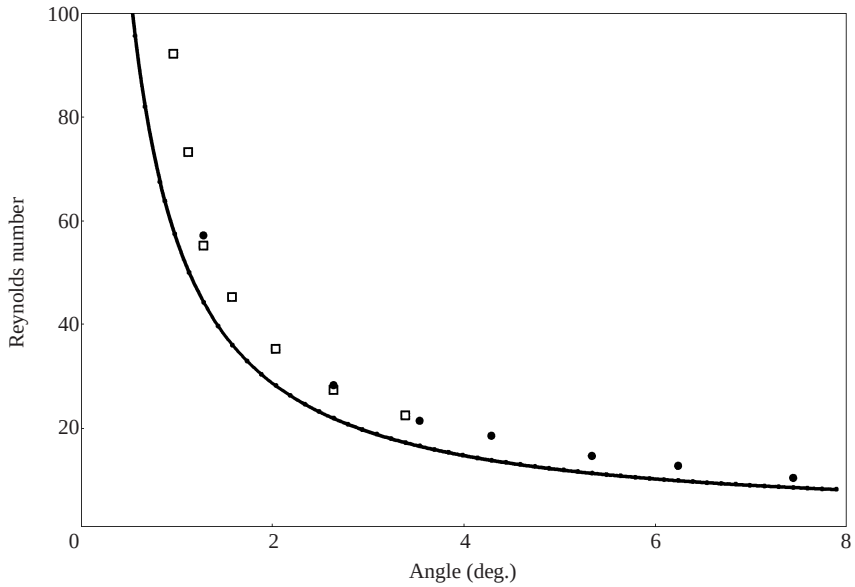

FIGURE 4. The neutrally stable Reynolds number, measured as a function of inclination angle for the orthogonal corrugated wall used: □, $Ka = 3365$; ●, $K\alpha = 1102$; ——, the neutrally stable Re for a flat wall.

With increasing Re, the free surface is observed to develop a static deformation, in agreement with asymptotic and numerical steady solutions (Bontozoglou & Papapolymerou 1997; Trifonov 1998*a*). Examination of the shape of the free surface provides information about the intensity of the wall/surface interaction. The free surface profile in the static flow regime is always periodic with the same wavelength as the wall corrugations but with an amplitude and phase that depend on the Reynolds number and inclination angle. Although the static flow regime is unstable in most of the parameter space (except for very small inclinations), its characteristics determine much of the dynamics of the other flow regimes.

The transition from a statically deformed to a spatio-temporally evolving free surface with increasing Re, occurs in stages. First, we observe a time-periodic variation of the amplitude of the deformed free surface and of the phase shift between the free surface and the wall. At higher Re, the unstable free surface gives way to travelling waves superimposed on the base static deformation. With a further moderate increase of Re, the waves depart from two-dimensionality and evolve into groups of 'horse-shoe waves'.

A most striking feature of the flow at higher Reynolds numbers is the establishment of a three-dimensional structure consisting of arrays of periodic, transverse depressions. The depressions are essentially confined to the troughs of the primary static free surface, and are quasi-static, exhibiting small-scale oscillations about fixed positions. The development of this transverse modulation leads to a stabilization of the system, demonstrated by the decrease in mean film thickness and the recession of travelling disturbances.

A flow regime map summarizing the above observations in terms of Reynolds number and inclination angle is shown in figure 5. The lower continuous line is the limit of linear stability and the upper continuous line marks the onset of the periodic three-dimensional structure. We are confident that both limits are independent of the

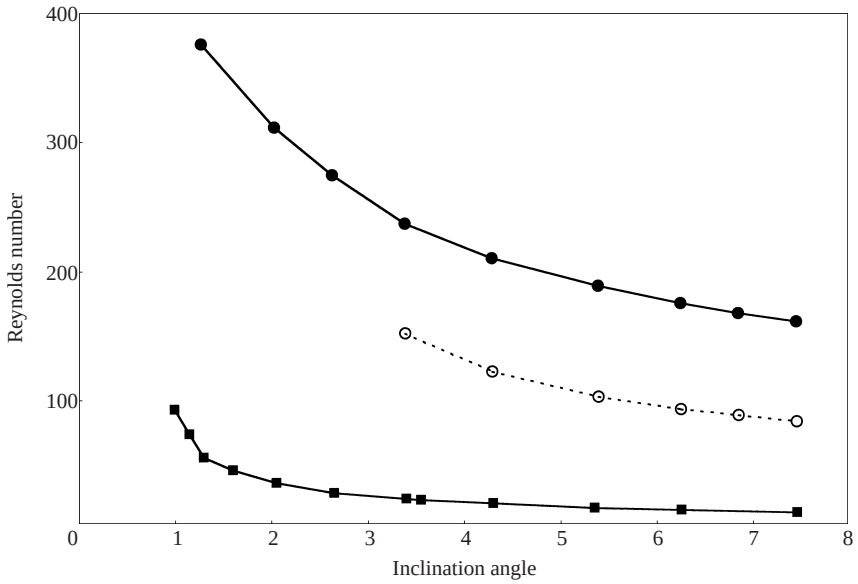

FIGURE 5. The flow regime map: –■–, linear stability limit; –●–, onset of transverse depressions; --○--, appearance of solitary waves.

length of the experimental setup. The intermediate, dashed line represents the first appearance of well-developed solitary pulses in the limited length of our channel. Below this line, the entire flow domain is characterized by the modulated static deformation of the free surface. This boundary depends on the channel length and is expected to approach the linear stability curve for a long enough channel. Documentation and detailed information on each of the aforementioned flow regimes is provided in the following sections.

5. Free surface with static deformation

The static flow regime is characterized by a two-dimensional and time-independent free surface. For $Re \sim O(10^0$–$10^1)$, the free surface is practically flat. Direct identification of the free surface location by a conductivity probe is thus straightforward (the probe consists of a needle attached to a displacement micrometer and its operation is based on the establishment of an electrical circuit as soon as the needle touches the surface of the liquid). Measurements under these conditions have shown that the film thickness over the crest of the wall is – to an accuracy of $\pm 10\,\mu$m – equal to the Nusselt film thickness. Thus, the shallow grooves across the wall do not affect the flow in this range of Reynolds numbers.

On the other hand, films with $Re \sim O(10^2)$ deviate significantly from the Nusselt flow. At the beginning of the channel, the free surface is two-dimensional and time-independent but develops a wavelength equal to that of the wall corrugations. An inspection of the stability curve (figure 4) suggests that, for $Re \sim O(10^2)$, the static flow regime with a deformed free surface is unstable for all but the smallest inclinations. However, the steady solution with a static free surface is not without practical significance, for the following two reasons: first, it persists, up to the highest Re examined, at the first 4–8 wavelengths of corrugation (in the rest of the text this part of the channel is designated as position A); second, its characteristics determine

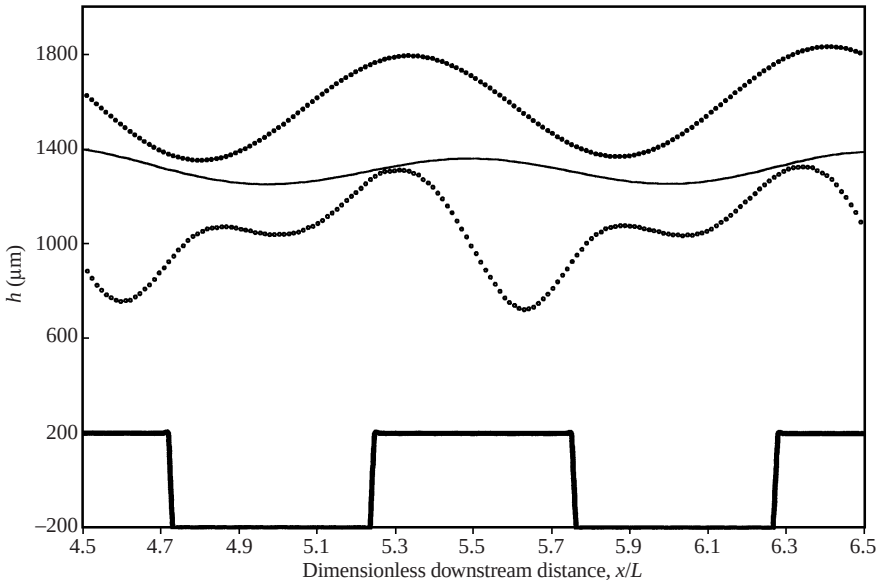

FIGURE 6. The variation with Re and φ of the amplitude and phase of the statically deformed free surface of water films. Roughly sinusoidal free surface at $\varphi = 1.3^\circ$ and $Re = 192$ (—) and 344 (●), and highly distorted free surface at $\varphi = 3.4^\circ$ and $Re = 297$ (○).

much of the dynamics of the other flow regimes. Therefore, the steady solution is studied in detail by systematically collecting data at position A. Line profiles, taken along the flow direction at different distances from the channel centreplane and at different time instants coincide, confirming that the flow at position A is steady and two-dimensional.

The statically deformed free surface is characterized by its amplitude, phase and harmonic content (for non-sinusoidal shapes, the amplitude is defined as half the normal distance from trough to crest and the phase refers to the fundamental harmonic). Figure 6 presents typical free surface profiles, which demonstrate the variation of these characteristics with Reynolds number and inclination angle.

The dependence of the free surface amplitude at position A on Reynolds number, is shown for different inclination angles in figure 7 and indicates an exponential increase. Measurements for pure water and for 26% by weight solution of glycerol in water are included, and a scaling – in terms of the Kapitsa number – is chosen, which brings together the respective data for the two liquids. In fact, curves corresponding to different inclination angles can be made to collapse by simple horizontal translation. Taking as reference a specific inclination, for example $\varphi_0 = 1.3^\circ$, this transformation can be accomplished by the empirical scaling of the x-coordinate $[ReKa^{-0.4} + (1/0.2)\ln(\varphi/\varphi_0)]$. The data in figure 7 also show that the growth of the free surface amplitude with Re stops abruptly at a value on the order of 500–600 μm, irrespective of inclination. With further increase in Re, the amplitude decreases slightly and then remains constant. This sudden transition corresponds to the establishment further downstream of the three-dimensional flow, whose characteristics will be described in detail later.

The variation of the phase of the free surface relative to the wall is shown as a function of Reynolds number in figure 8 (actually computed is the difference in phase between the fundamental harmonic of the free surface and that of the wall). With

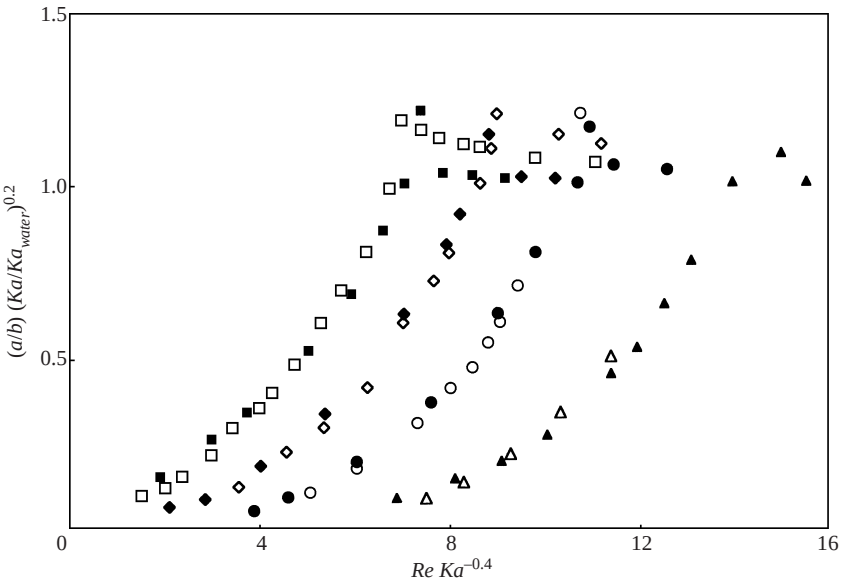

FIGURE 7. The ratio of free surface amplitude to wall amplitude, scaled with the Kapitsa number, as a function of the dimensionless group $ReKa^{-0.4}$. Data are presented for inclination angles: $\varphi = 1.3°$ (▲, △), 2.6° (●, ○), 3.4° (◆, ◇) and 5.4° (■, □). Open symbols refer to 26% wt. glycerol solution and filled symbols to pure water.

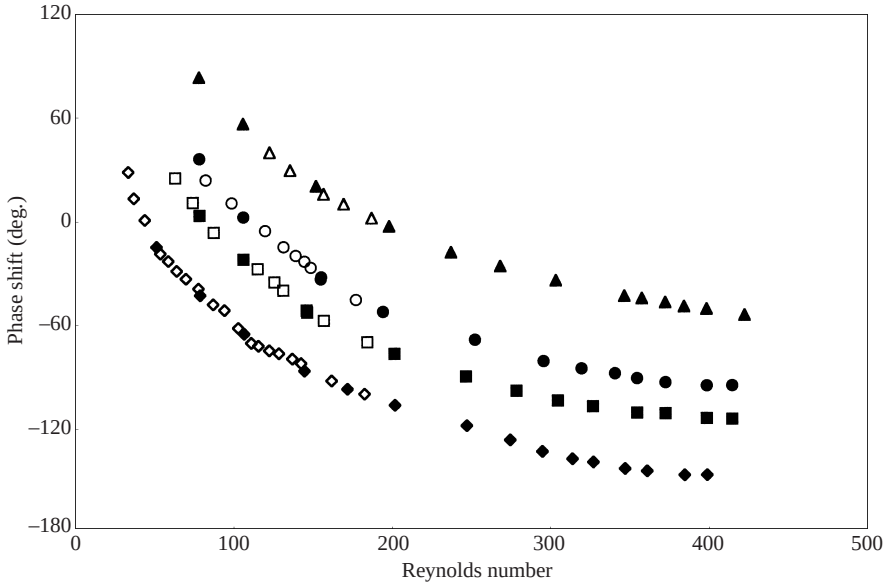

FIGURE 8. The phase shift between the free surface and the corrugated wall as a function of *Re* for inclination angles: $\varphi = 1.3°$ (▲, △), $\varphi = 2.6°$ (●, ○), $\varphi = 3.4°$ (■, □) and $\varphi = 5.4°$ (◆, ◇). Open symbols refer to 26% wt. glycerol solution and dark symbols to pure water.

increasing *Re*, the free surface is observed to lag behind the wall corrugations and to asymptotically approach a constant position that depends on inclination angle. Data for the two liquids used in the present work fall on the same curve, indicating that – unlike for the previously discussed effect on amplitude – there is no dependence on

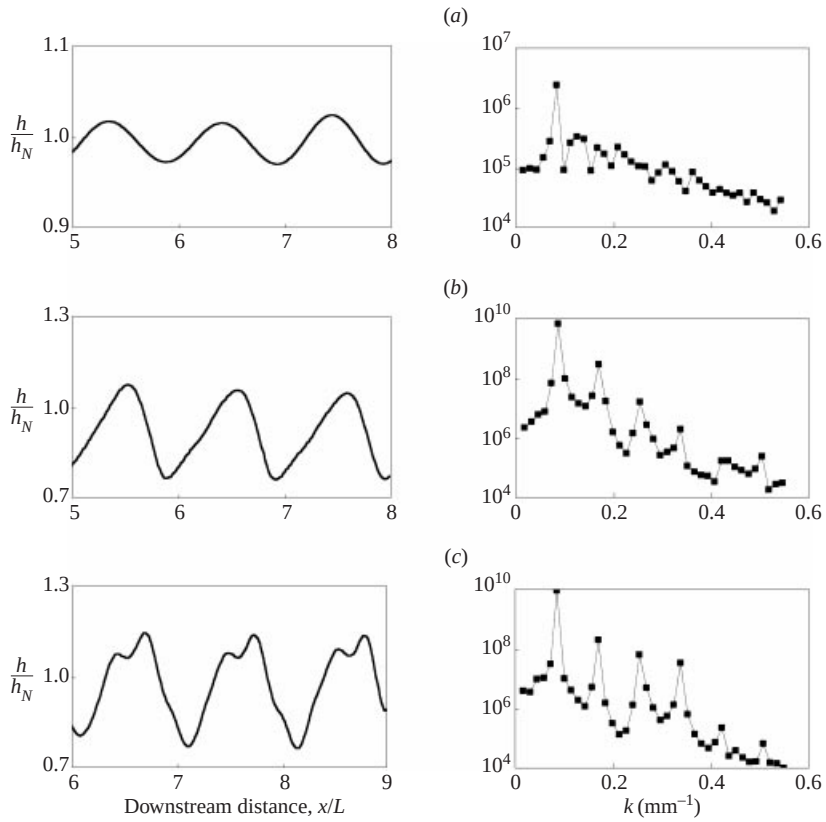

FIGURE 9. The harmonic content of the static free surface as a function of *Re*. Line profiles along the flow direction at (*a*) $Re = 135$, (*b*) $Re = 235$ and (*c*) $Re = 290$ and the corresponding spatial power spectra.

Kapitsa number. Again, curves corresponding to different inclination angles can be made to collapse by simple vertical translation.

Next, we consider the harmonic content of the static free surface, which is observed to be a strong function of the Reynolds number. At small *Re* the free surface is practically sinusoidal, whereas at large *Re* higher harmonics become significant, resulting in line profiles with ripples. An example of this trend is depicted in figure 9 for $\varphi = 2.6^\circ$ and $Re = 135$, 235 and 290. Also shown are spatial power spectra of the line profiles, which confirm the appearance of higher harmonics. In particular, in the last case the harmonics corresponding to wavelengths $\lambda_2 = 6\,\text{mm}$, $\lambda_3 = 4\,\text{mm}$ and $\lambda_4 = 3\,\text{mm}$ have comparable amplitudes.

At this point, we shall compare the experimental results on the static deformation of the free surface to the linear predictions of Bontozoglou & Papapolymerou (1997) and the computational predictions of Bontozoglou (2000). The first authors have found a weak resonant interaction between the free surface and a sinusoidal wall of infinitesimal amplitude, which occurs at a specific Reynolds number, Re_{cr}, depending on inclination. Apart from the Reynolds number, other dimensionless groups derived from their analysis are the dimensionless wavenumber, $k = 2\pi h/L$, and a modified Bond number $B = 4\pi^2\sigma/\rho g_x + g_y/g_x$. However, a closed-form relation between these numbers and the resonant conditions was not reported.

Computation of the steady flow over finite-amplitude sinusoidal corrugations by

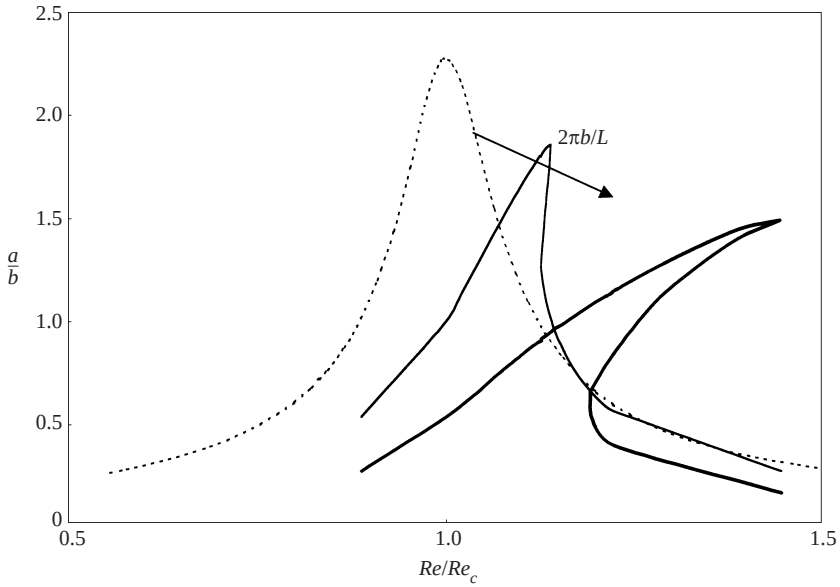

FIGURE 10. A qualitative plot of the free surface amplification of sinusoidal wall corrugations (ratio of the thee surface amplitude to that of the wall), as a function of *Re*. The dashed line corresponds to linear analysis valid for infinitesimal corrugations, and the continues lines represent the outcome of numerical computations for corrugations of finite amplitude.

Bontozoglou (2000) – using a pseudo-spectral numerical scheme – revealed that the resonance curve of free surface amplitude versus *Re* has the typical supercritical shape, including a triple-valued range. The variation of the resonance curve with increasing corrugation amplitude is shown qualitatively in figure 10. It suggests that, for finite-amplitude corrugations, the linear resonant Reynolds number, Re_{cr}, corresponds more closely to the onset of the parametric region with highly distorted free surface than to its maximum value.

To test the above asymptotic and numerical predictions, we need to single out from the data the effect of the fundamental harmonic of the wall (the corrugated wall of the present experiment is not monochromatic but may be considered to consist of the Fourier series of superharmonics of the fundamental $\lambda_1 = 12\,\text{mm}$). Thus, we take the power spectrum (spatial Fourier transform) of the measured free surface deformations and plot the magnitude of the fundamental harmonic as a function of the Reynolds number. Data for four inclination angles and $50 < Re < 400$ are shown in figure 11. Marked by circles are the values of Re_{cr} from linear theory for each inclination angle considered. A very satisfactory correlation of Re_{cr} with the onset of steep ascent of the fundamental free surface harmonic is observed in all cases. This finding provides a strong argument in support of the predictions of linear theory.

Finally, it is of interest to trace the origin of the superharmonics that develop on the free surface at high Reynolds numbers. In particular, we would like to know whether their excitation reflects predominantly the linear effect of the respective wall superharmonics or whether it is a manifestation of nonlinearity. To this end, we consider the magnitude of the first, second and third superharmonics of the free surface as a function of *Re*. The results for inclination $\varphi = 3.4^\circ$ are plotted in figure 12. Also marked are the predictions of linear theory for sinusoidal wall corrugations with respective wavelengths 12 mm, 6 mm, 4 mm and 3 mm, which correspond to the

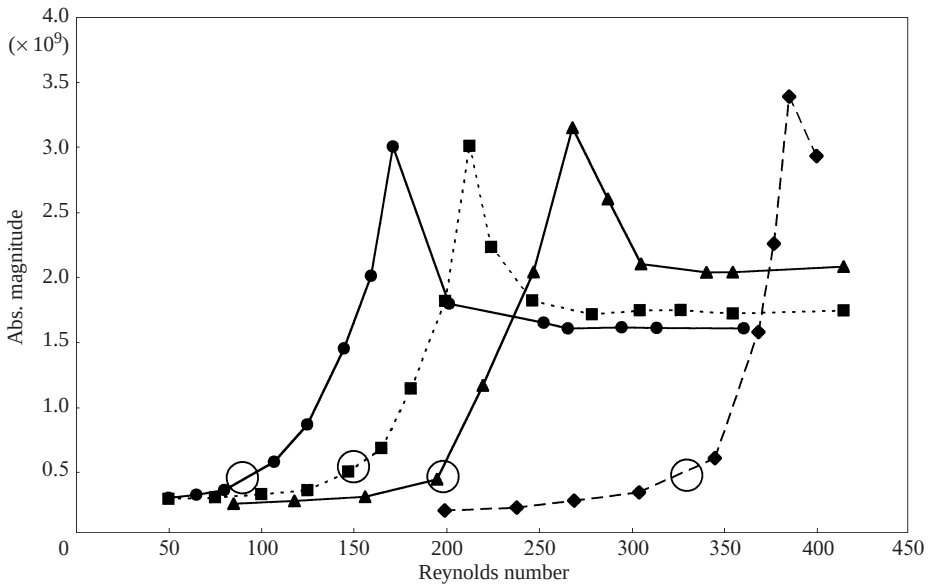

FIGURE 11. The amplitude of the fundamental harmonic of line profiles at position A as a function of *Re*. Data are presented for water and inclination angles $\varphi = 1.3°$ (◆), 2.6° (▲), 3.4° (■) and 5.4° (●). Marked by circles are the resonance values, Re_{cr}, predicted for the respective angle by linear theory.

fundamental and the superharmonics. Again a very satisfactory correlation of Re_{cr}, with the onset of steep ascent of each superharmonic is observed. Thus, we are led to the conclusion that the harmonic content of the deformed free surface at high Reynolds numbers is, to first order, a result of the non-sinusoidal shape of the periodic wall.

6. Onset and evolution of progressive waves

Having determined the characteristics of the base flow (as clearly observed at position A close to the channel entrance), we proceed to describe the appearance and growth of travelling disturbances selectively amplified by the flow system from ambient noise. Thus, systematic triggering, such as an inlet disturbance of specific frequency, is not applied. However – as will be shown below – the spatial forcing imposed by the periodic wall results in a much sharper selection process compared to film flow along a flat wall with the same disturbance level.

It was previously noted that, with increasing Reynolds number, the static deformation regime is eventually restricted to the first 4–8 corrugation wavelengths. This behaviour is borne out by the data in figure 13, which indicate the downstream location where the free surface first deviates from the static form. Data for the two viscosities examined confirm that the transition is satisfactorily described by the Reynolds number. The next stage of downstream evolution involves a gradual growth in the amplitude of the deformed free surface, accompanied by a time-oscillation of this amplitude around the growing mean value. Figure 14 shows the mean free surface amplitude as a function of downstream distance for channel inclination $\varphi = 2.6°$ and various Reynolds numbers. The growth in mean amplitude with downstream distance is rather gradual at the smallest *Re* plotted, and this flow regime may cover almost

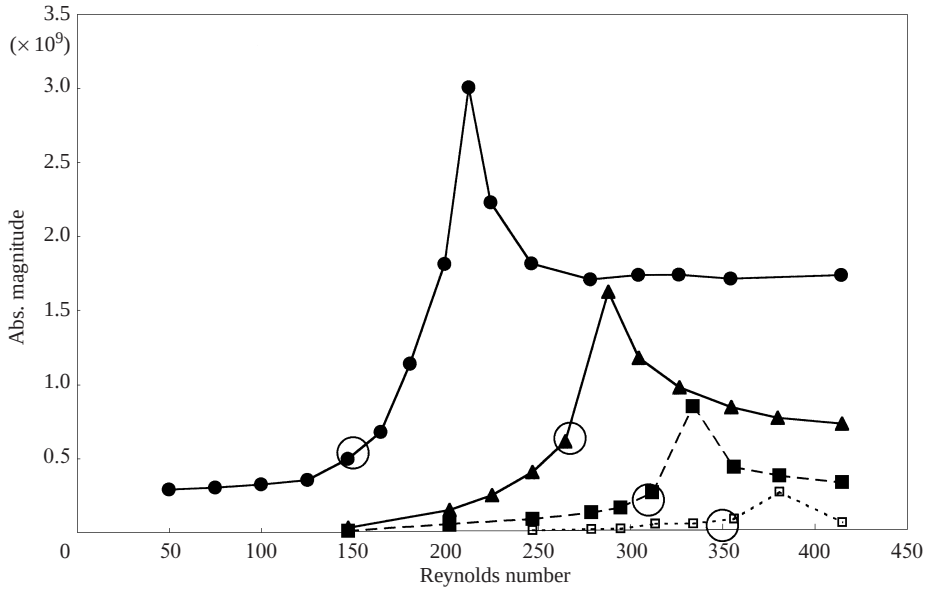

FIGURE 12. The amplitude of the fundamental (●) and the first (▲), second (■) and third (□) superharmonic of the free surface as a function of *Re*. Data for water and inclination angle $\varphi = 3.4°$. Marked by circles are the resonance values, Re_{cr}, predicted for the respective wavelength by linear theory.

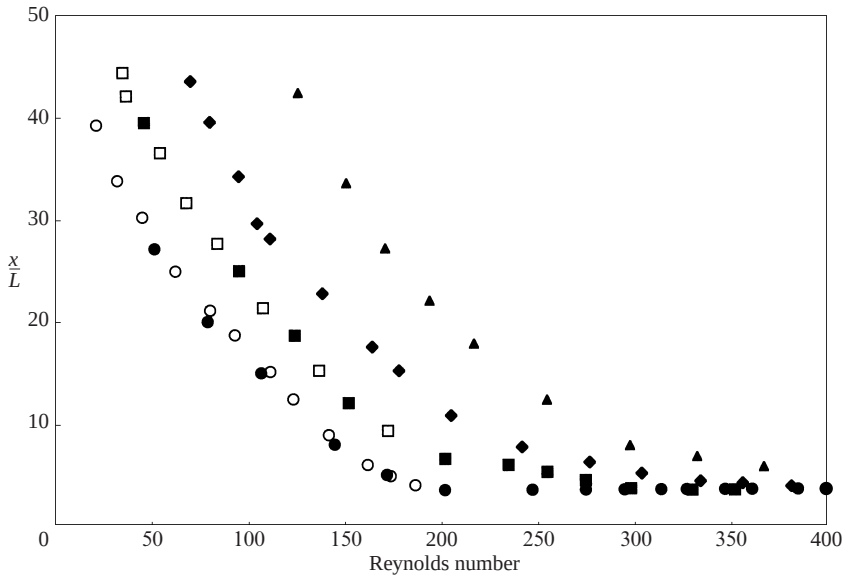

FIGURE 13. The downstream location where the free surface first deviates from the static form as a function of *Re*, for inclination angles: $\varphi = 1.3°$ (▲), 2.6° (◆), 3.4° (■, □) and 5.4° (●, ○). Open symbols correspond to 26% wt. glycerol solution and filled symbols to pure water.

the entire length of the available corrugated section of the channel. In contrast, at higher *Re* there is a fast approach to constant mean amplitude. For example, figure 14 shows that, in the range of $265 < Re < 310$, the transient length does not exceed 3–4 corrugations (36–48 mm).

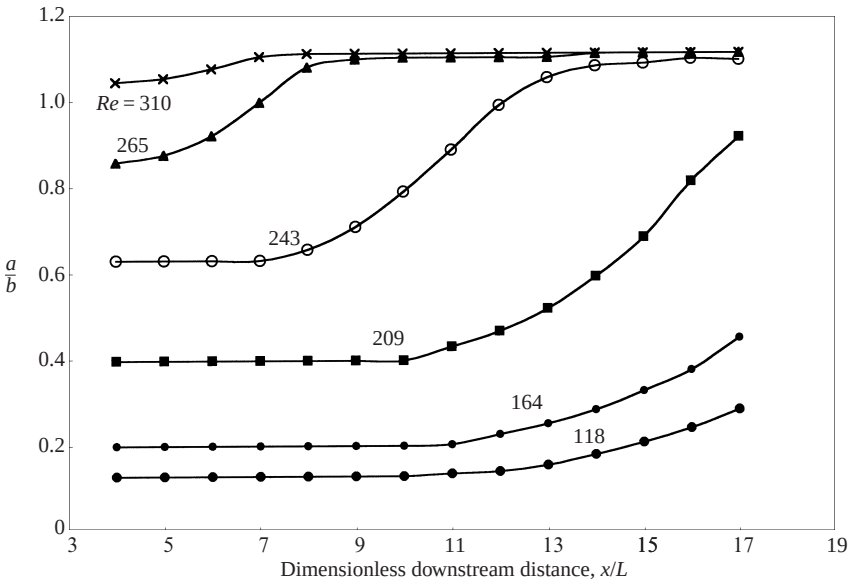

FIGURE 14. The mean free surface amplitude as a function of downstream distance for water films at inclination angle $\varphi = 2.6^\circ$ and various Reynolds numbers.

Next, we examine the characteristics of the temporally oscillatory part of the flow and its downstream evolution. In particular, we note the following effect of the Reynolds number when observing the free surface elevation at a fixed location: at first, only the amplitude oscillates appreciably; then, with increasing Re the phase of the free surface also oscillates, and finally a similar time-dependent variation of the higher harmonic content of the free surface becomes evident.

To examine the frequency range of this time-variation, we follow two complementary procedures. First, we form the time-series of the free surface position at a specific downstream location and apply the FFT routine to obtain the discrete Fourier transform. Second, we consider at each time instant the entire streamwise line profile of the 85 mm view window and decompose it by a spatial Fourier transform to obtain the instantaneous value of the amplitude and phase of the fundamental harmonic. Repeating the procedure for each time instant, we form the time-series of these two quantities and examine their frequency content by taking the temporal Fourier transform (this combination is occasionally called spatio-temporal Fourier transform).

The outcome of both procedures is qualitatively the same and representative examples are shown in figure 15(a, b). More specifically, a time-series of the free surface elevation at a downstream location $x_0 = 28L$ is shown for $\varphi = 2.6^\circ$ and $Re = 209$ in figure 15(a) together with its temporal spectrum. In figure 15(b) a time-series of the magnitude of the fundamental harmonic is depicted, together with its power spectrum, both corresponding to a streamwise line profile taken at the same location and under the same conditions as those in figure 15(a). The frequency of our image grabbing system ($f = 20$ Hz) permits reliable representation of the major features of the spectra in the frequency range depicted, but is evidently not high enough to resolve fine details.

The most notable conclusion drawn from figures 15(a) and 15(b) is that the time variation of all the quantities is confined to a rather narrow frequency interval around

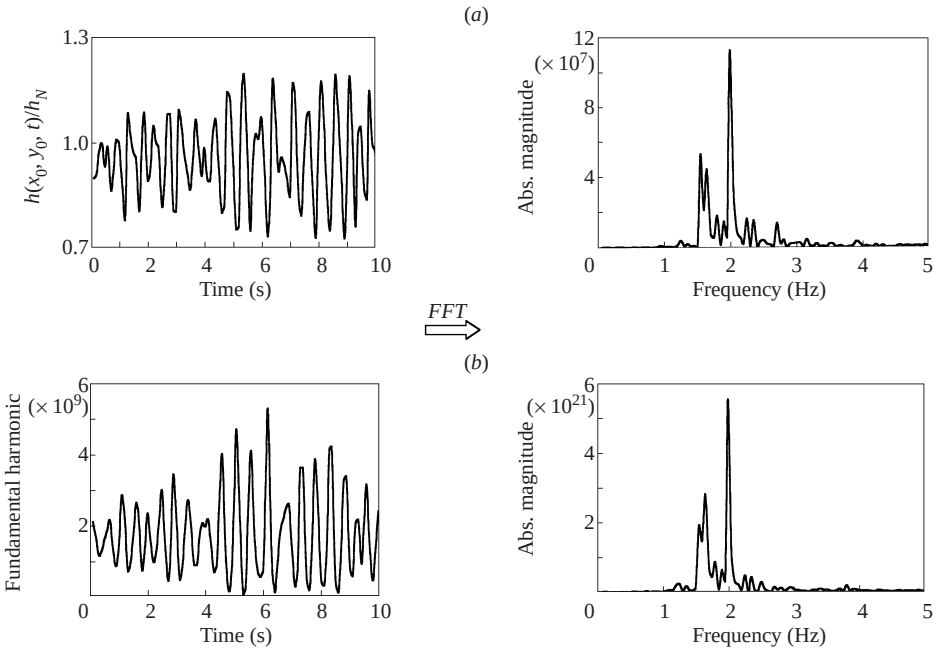

FIGURE 15. (*a*) A time-series of the free surface elevation $h(x_0, y_0, t)$ at the centreline ($y_0 = 0$) and downstream locations $x_0 = 28L$, in a flow with $\varphi = 2.6°$, $Re = 209$, $Ka = 3365$, and the corresponding temporal discrete Fourier transform. (*b*) A time-series of the magnitude of the fundamental harmonic (the outcome of a spatial Fourier transform of the original line profile, taken at the same location and under the same conditions as (*a*)) and the corresponding temporal discrete Fourier transform.

2 Hz. A similar transformation of the phase of the fundamental harmonic (not shown) indicates that it also oscillates in synchrony with the amplitude at the above frequency range. This behaviour is completely different from the results of film flow over a flat wall, where – in the absence of an external regular disturbance – the power spectrum is very broad and cannot be characterized by any single frequency.

The source of the observed time-oscillatory behaviour is concealed by the dominant static deformation imposed on the free surface by the wall. To remove the latter, we consider each instantaneous line profile and take a moving spatial average over the length of 12 mm (i.e. the length scale imposed by the corrugations). In this way, the fundamental quasi-static deformation is to a large extent removed, and the transformed line profiles retain only the spatial variation related to longer scales. Five consecutive line profiles (displaced vertically for clarity) are shown in figure 16(*a*), and the outcome of the moving spatial average is shown in figure 16(*b*). Both figures indicate the passage of long, progressive waves. In particular, the first profile depicts the substrate in front of the wave, the next two depict the passage of the wave crest through the viewing window and the final two correspond to the wave tail. We conclude that the frequency content recorded above reflects precisely the frequency spectrum of these travelling disturbances.

Based on the above, the following plausible explanation of the synchronous oscillation in amplitude and phase of the fundamental spatial harmonic is suggested: According to the observations described in § 5, the fundamental amplitude and phase are functions of the Reynolds number or, equivalently, of the film thickness. The slow variation in film thickness caused by the travelling disturbances imposes quasi-

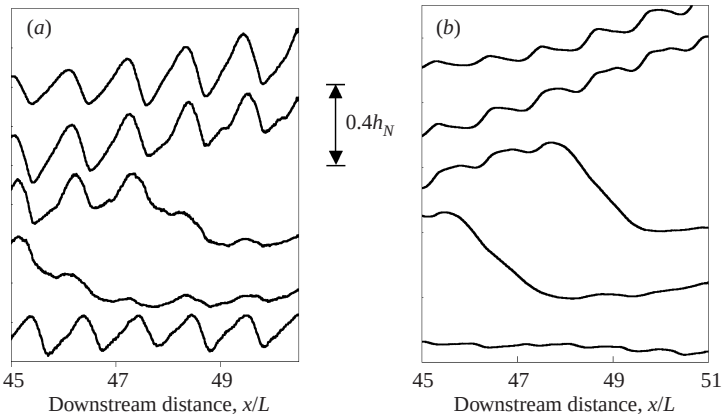

FIGURE 16. (*a*) The passage of a fully developed solitary wave over the corrugated wall in a flow with $Re = 102$, $\varphi = 5.4^\circ$ and $Ka = 1102$. Five consecutive line profiles are Shown, displaced vertically for clarity. (*b*) The outcome of a moving spatial average over the length of 12 mm for the line profiles in (*a*).

equilibrium conditions, whereby the characteristics of the statically deformed free surface continuously conform to the prevailing film thickness.

The occurrence of a sharper selection process (in comparison to film flow along a flat wall), which results in travelling disturbances within a narrow frequency range, is demonstrated by the change of the power spectrum of the free surface elevation with downstream distance. The data in figure 17 are taken with the 26% glycerol solution at $\varphi = 5.4^\circ$, $Re = 115$ and show the spectra at locations $x_0 = 15L$, $35L$ and $45L$. A gradual concentration of the frequency content around 1.5–2.0 Hz is evident. We also note that the last spectrum corresponds to fully developed solitary waves.

Next, we proceed to a visual demonstration of the characteristics of fully developed solitary waves over the corrugated wall, using a high-speed video camera. With increasing Reynolds number, the first waves observed in our short channel appear as shown in figure 18(*a*). The waves have their crests aligned at right angles to the streamwise direction, apart from a slight curvature known to occur because of the sidewalls. The only differences, in comparison to solitary waves over a flat wall, are that the former are very regular (reminiscent of waves produced by inlet disturbances of controlled frequency), and that they override the statically deformed free surface. This last observation is supported by streamwise line profiles such as the ones shown in figure 16(*a*).

A major change takes place with increasing Reynolds number or, equivalently, increasing inclination angle: the solitary waves become oblique. More specifically, the direction of propagation forms an angle with the streamwise direction, and this varies between successive crests as documented in figure 18(*b*). With further increase in Reynolds number or inclination angle, the oblique crests combine to form waves with highly curved fronts (figure 18*c*). The evolution under more intense conditions is depicted in figure 18(*d*, *e*, *f*) and involves an increase in the number and sharpness of these 'horseshoe waves'. The resulting free surface structure is similar to that observed in fully developed vertical falling films along a flat wall (Adomeit & Renz 2000).

The existence of a narrow frequency range for the first naturally generated solitary waves, as well as the subsequent formation of oblique waves, point to the possibility of triad wave interactions whereby energy is transferred from the statically deformed

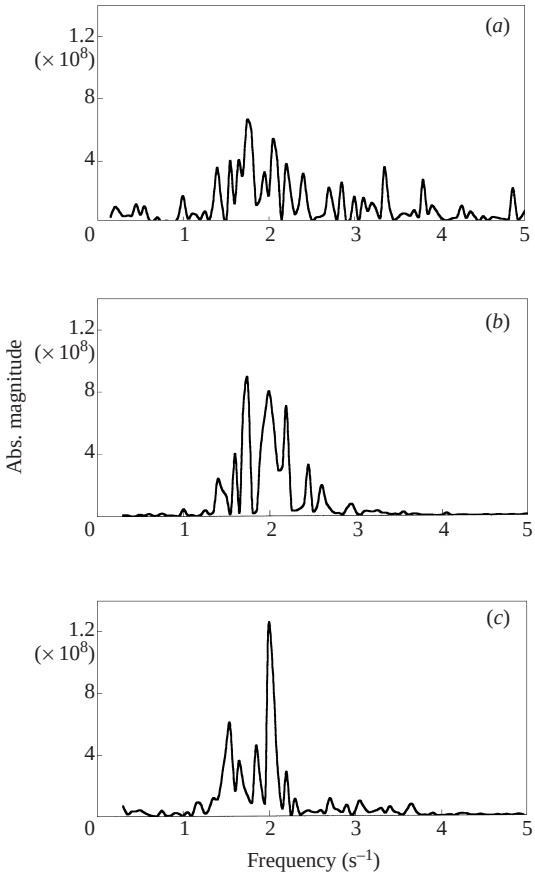

FIGURE 17. The evolution with downstream distance of the power spectrum of free surface elevation $h(x_0, y_0, t)$, for a flow with $\varphi = 5.4°$, $Re = 115$ and $Ka = 1102$. Data are taken along the centreline and at downstream locations: (*a*) $x_0 = 15L$, (*b*) $x_0 = 35L$ and (*c*) $x_0 = 45L$.

free surface to the travelling disturbances. A similar mechanism has been thoroughly investigated in the problem of Bragg scattering of ocean waves by bottom topography (Davies & Heathershaw 1984; Mei 1985).

7. Transition to three-dimensional flow

In the previous section we have described travelling waves (solitary-like pulses) produced without imposing any kind of systematic perturbation. In the case of flow over a flat wall, the strongly nonlinear two- and three-dimensional dynamics of these solitary waves and their interactions are of primary importance in the further evolution towards a fully turbulent film flow (Liu & Gollub 1994; Chang 1994). However, a qualitatively different high-*Re* transition occurs in the film flow along a periodic wall analysed here. This transition suppresses travelling waves and stabilizes the flow above a critical Reynolds number.

In the experiments with water, a quasi-steady three-dimensional flow is established above a certain liquid flow rate, which consists of arrays of periodic depressions and elevations in the transverse direction. When the transition sets in, it is observed to spread over most of the channel area (with the exception for the first few corrugations),

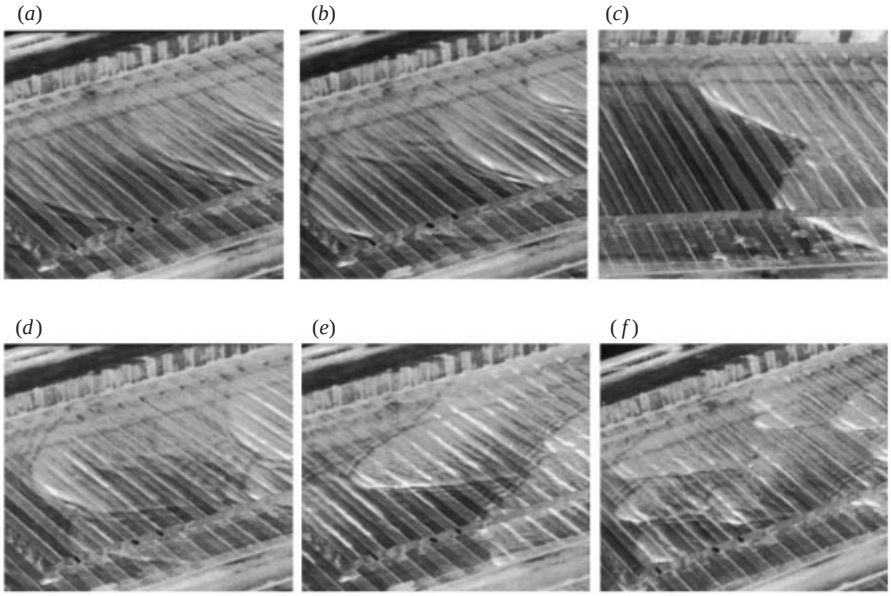

FIGURE 18. Visual records of solitary waves for different parametric conditions (Re, φ) taken by a high-speed video camera. (a) $\varphi = 3.4°$, $Re = 175$; (b) $\varphi = 3.4°$, $Re = 225$; (c) $\varphi = 5.4°$, $Re = 125$; (d) $\varphi = 5.4°$, $Re = 165$; (e) $\varphi = 7.4°$, $Re = 145$; (f) $\varphi = 7.4°$, $Re = 175$.

a behaviour indicative of absolute instability. The spatial structure of the three-dimensional pattern is better illustrated by processing the original digitized frames to produce iso-contours of constant free surface elevation. Such results are shown in figures 19(a) ($\varphi = 1.3°$, $Re = 380$) and 19(b) ($\varphi = 2.6°$, $Re = 355$), where darker regions correspond to depressions and lighter to elevations. The position of the wavy wall is also indicated at the bottom of the figures, and helps to clarify that the depressions are located at the troughs of the wall corrugations and the elevations are at the crests.

Except for the lowest inclination angle examined, the three-dimensional pattern is almost static, with the depressions executing transverse oscillations of very small amplitude about a fixed mean position. In the exceptional case of $\varphi = 1.3°$, the depressions are observed to travel towards one of the sidewalls of the channel. Their speed is everywhere approximately the same, but the direction of travel, though uniform inside a specific trough, changes in an apparently random fashion among successive troughs.

Increasing the inclination angle results in the appearance of the three-dimensional structure at lower flow rates. Also, the free surface is characterized by smaller length scales. This change is qualitatively evident when comparing figures 19(a) and 19(b). In the latter figure, depressions and elevations are more closely spaced in the transverse direction, and new local extrema appear in the streamwise direction. A more systematic presentation of the changes with inclination is offered by the line profiles depicted in figure 20(a, b). Figure 20(a) shows roughly sinusoidal line profiles in the transverse direction, which exhibit a gradual decrease in wavelength with inclination. Figure 20(b) compares streamwise line profiles for flows with inclination 1.3° and 2.6°. The lower free surface is evidently more distorted by higher harmonics, which correspond to the subsidiary extrema observed in figure 19(b).

The appearance of the three-dimensional flow structure results in a remarkable

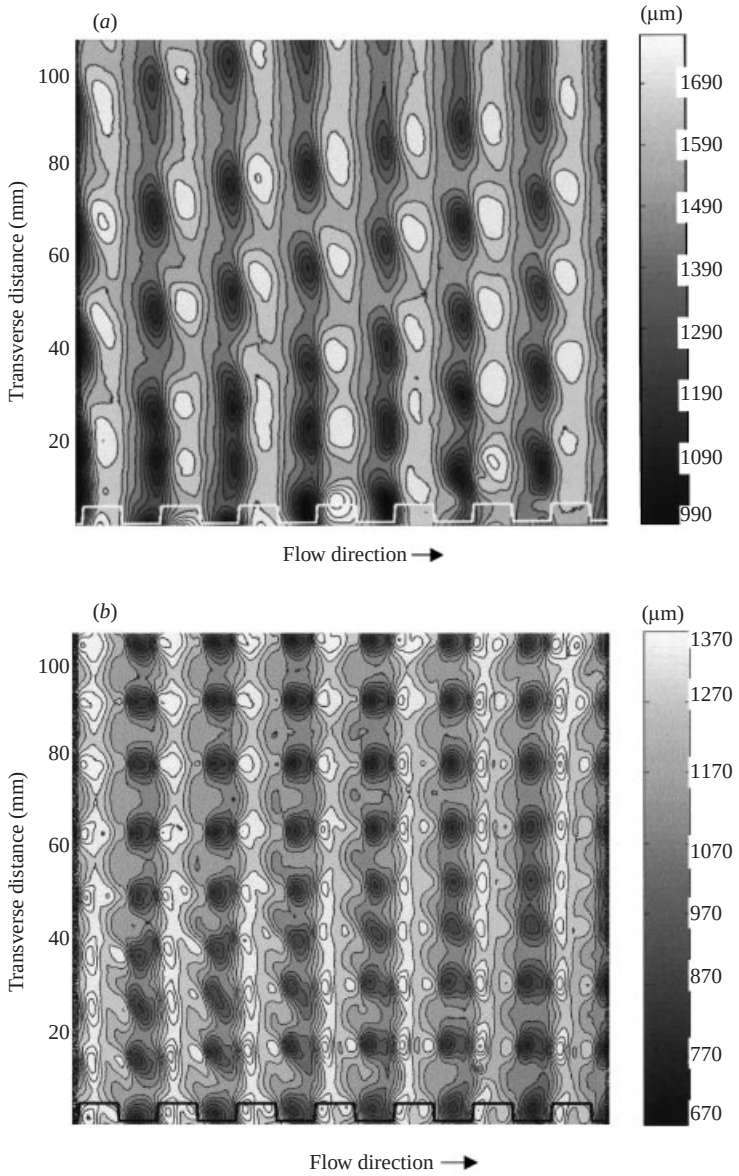

FIGURE 19. Iso-contours of constant free surface elevation in two flows with water, indicating the appearance of a three-dimensional pattern. (*a*) $\varphi = 1.3°$, $Re = 380$; (*b*) $\varphi = 2.6°$, $Re = 355$.

stabilization of film flow. Two manifestations of this stabilization are the recession of the naturally excited solitary waves and a strong departure of mean film thickness from the Nusselt prediction. The former observation is in contrast with the behaviour at flow rates slightly below the critical for three-dimensional transition, where fully developed solitary pulses are observed to form at small distance (100–200 mm) from the entrance section. With the appearance of the transverse depressions, the solitary waves are almost eliminated, and this early and drastic change in the flow is an additional indication that the transition is independent of the channel length.

The departure from Nusselt prediction is documented in figure 21(*a*), where the

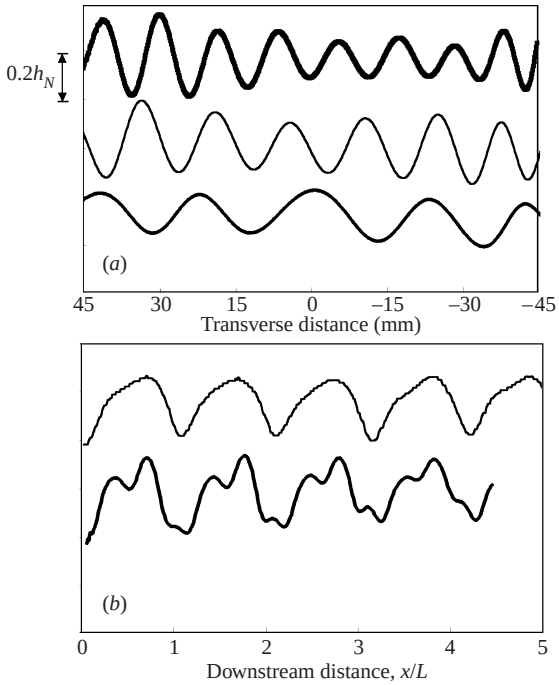

FIGURE 20. (*a*) Transverse line profiles along a trough of the wall, in flows with water and $\varphi = 1.3°$, $Re = 400$ (upper curve), $\varphi = 2.6°$, $Re = 370$ (middle curve) and $\varphi = 3.4°$, $Re = 330$ (lower curve). (*b*) Streamwise line profiles in flows with water and inclination $\varphi = 1.3°$, $Re = 380$ (top curve) and $\varphi = 2.6°$, $Re = 355$ (bottom curve).

measured mean film thickness – defined as the average distance from the level of the corrugation crests up to the free surface – is plotted as a function of the Nusselt film thickness. At every inclination angle there is a clearly defined transition point above which the data depart drastically from the Nusselt prediction (a decrease in mean film thickness with flow rate is even observed for a short range of flow rates just after transition). These transition points coincide with the establishment of the three-dimensional flow pattern, and define the boundary of the respective regime in the flow regime map (figure 5) introduced in § 4.

The aforementioned transverse depressions on the free surface of the liquid film appear only in water. This observation is in accord with common experience that high viscosity suppresses three-dimensional instabilities (see for example Liu, Scheider & Gollub 1995). However, though no appreciable three-dimensional structure is recorded on the free surface of the 26% glycerol solution film, similar stabilization phenomena are manifested and a transition is clearly identified from the corresponding data of mean film thickness, shown in figure 21(*b*). (It would be of interest to investigate – by taking velocity measurements inside the film – whether a three-dimensional flow field is actually established, with the high viscosity simply attenuating its manifestation at the free surface.)

The present results on three-dimensional transition at high flow rates can be combined with previously reported measurements at position A of the channel, where the statically deformed free surface persists (§ 5). In particular figure 7 demonstrates that, beyond a certain value of the Reynolds number (dependent on inclination), the amplitude of the statically deformed free surface abruptly stops growing exponentially

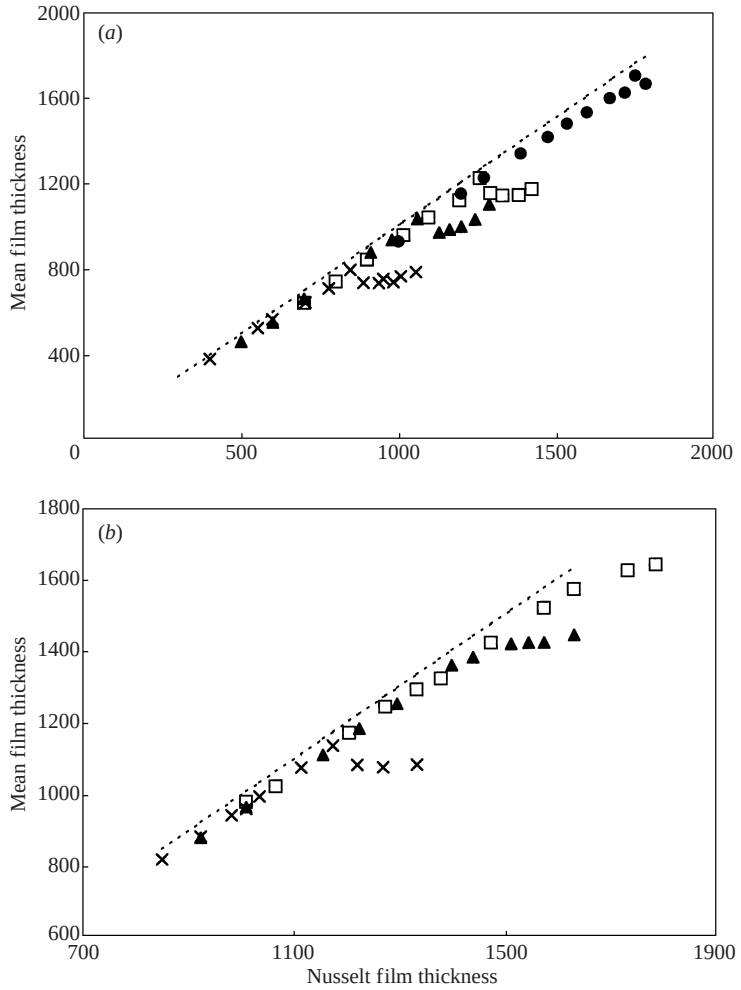

FIGURE 21. Measured mean film thickness as a function of Nusselt film thickness. (*a*) Data for water and inclination angles 1.3° (●), 2.6° (□), 3.4° (▲), 5.4° (×). (*b*) Data for 26% wt. glycerol in water and inclination angles 2.6° (□), 3.4° (▲) and 5.4° (×).

and settles at a roughly constant value. This transition of the static profile at position A of the channel is found to coincide with the establishment of the three-dimensional regime further downstream. The coincidence supports the idea that the present flow structure is the outcome of a secondary, three-dimensional instability excited when the streamwise profile of the primary steady flow exceeds a certain steepness. It is conjectured that the three-dimensional pattern actually bifurcates from the upper turning point of the nonlinear resonance curve sketched in figure 10, which corresponds to the transition from sub-critical to super-critical flow.

8. Conclusions

A fluorescence imaging method has been used to investigate the structure of gravity-driven film flow along a corrugated wall. Different flow regimes have been identified and their characteristics described. The steady flow regime, which exhibits a statically

deformed free surface with the same wavelength as the wall, is found to persist in the first few corrugation wavelengths and to influence the non-stationary dynamics in the rest of the channel. Its properties, i.e. the amplitude, phase and harmonic content of the free surface, are correlated by the Reynolds and Kapitsa numbers. These measurements are interpreted in terms of the wall/free surface resonant interaction proposed by Bontozoglou & Papapolymerou (1997).

Travelling disturbances are shown to destabilize the flow and evolve into solitary humps superimposed on the base flow. In the upstream part of the channel, travelling disturbances are dominated by the statically deformed free surface, and they are manifested only as oscillations in the amplitude and phase of the base pattern. Further downstream, fully developed solitary waves appear. At the lower *Re*, they exhibit a regular frequency, indicating that the spatial forcing imposed by the periodic wall results in a sharp and direct selection process. This behaviour is in contrast with the more indirect formation of solitary waves along a flat wall, which has been found by Liu & Gollub (1994) and Cheng & Chang (1995) to proceed through secondary subharmonic and/or sideband instabilities of the (initially short) fastest growing modes. At higher *Re* the waves become oblique and finally evolve into a staggered pattern of 'horseshoe waves' with highly curved fronts.

A unique feature of high-*Re* film flow along a corrugated wall is the establishment of a three-dimensional flow regime leading to the suppression of travelling waves and to a decrease in mean film thickness. In the experiments with water, this flow regime is further manifested by the formation of arrays of isolated depressions along the free surface in the transverse direction. Based on the concomitant arrest of the growth in amplitude of the statically deformed free surface (observed at the first wavelengths of the channel), we argue that the above pattern bifurcates from the two-dimensional base flow when it exceeds a certain steepness.

Further progress in this problem may be made in two directions. First, given that the present results refer to a single corrugation dimension, it is important to examine the dependence of the phenomena on the wavelength and amplitude of the corrugations. Such results may further elucidate the structure of the flow in the flow regimes identified here. In particular, variation of the wavelength of the corrugations is expected to provide insights on the effect of the free shear layers which form at the edges. Also, a change in the amplitude-to-wavelength ratio will influence the occurrence and extent of recirculating regions inside the cavities. A second direction of research could involve the more detailed investigation of the selection process imposed on random noise by the periodic wall. This could plausibly be accomplished by introducing controlled-frequency disturbances at the channel inlet.

This work was partly supported by the EU through INTAS Programme 99-1107.

REFERENCES

Adomeit, P. & Renz, U. 2000 Hydrodynamics of three-dimensional waves in laminar falling films. *Intl J. Multiphase Flow* **26**, 1183–1208.

Benjamin, T. B. 1957 Wave formation in laminar flow down an inclined plane. *J. Fluid Mech.* **2**, 554–574.

Bontozoglou, V. 2000 Laminar film flow along a periodic wall. *CMES – Comp. Model. Engng* **1**, 129–138.

Bontozoglou, V. & Papapolymerou, G. 1997 Laminar flow down a wavy incline. *Intl J. Multiphase Flow* **23**, 69–79.

Chang, H.-C. 1994 Wave evolution on a falling film. *Annu. Rev. Fluid Mech.* **26**, 103–136.

Cheng, M. & Chang, H.-C. 1995 Competition between sideband and subharmonic secondary instability on a falling film. *Phys. Fluids* **7**, 34–54.

Dassori, C. G., Deiber, J. A. & Cassano, A. E. 1984 Slow two-phase flow through a sinusoidal channel. *Intl J. Multiphase Flow* **10**, 181–193.

Davies, A. G. & Heathershaw, A. D. 1984 Surface-wave propagation over sinusoidally varying topography. *J. Fluid Mech.* **144**, 419–443.

Fair, J. R & Bravo, J. R. 1990 Distillation columns containing structure packing. *Chem. Engng Prog*. **86**, 19–29.

Focke, W. W. & Knibbe, P. G. 1986 Flow visualization in parallel-plate ducts with corrugated walls. *J. Fluid Mech.* **165**, 73–77.

Kang, F. & Chen, K. 1995 Gravity-driven two-layer flow down a slightly wavy periodic incline at low Reynolds numbers. *Intl J. Multiphase Flow* **21**, 501–513.

Liu, J. & Gollub, J. P. 1994 Solitary wave dynamics of film flows. *Phys. Fluids* **6**, 1702–1712.

Liu, J., Paul, J. D. & Gollub, J. P. 1993 Measurements of the primary instabilities of film flow. *J. Fluid Mech.* **250**, 69–101.

Liu, J., Schneider, J. B. & Gollub, J. P. 1995 Three-dimensional instabilities of film flows. *Phys. Fluids* **7**, 55–67.

Malamataris, N. T. & Bontozoglou, V. 1999 Computer aided analysis of viscous film flow along an inclined wavy wall. *J. Comput. Phys.* **154**, 372–392.

Mei, C. C. 1985 Resonant reflection of surface water waves by periodic sandbars. *J. Fluid Mech.* **152**, 315–335.

Pozrikidis, C. 1988 The flow of a liquid film along a periodic wall. *J. Fluid Mech.* **188**, 275–300.

deSantos, J. M., Melli T. R. & Scriven, L. E. 1991 Mechanics of gas-liquid flow in packed-bed contactors. *Annu. Rev. Fluid Mech.* **23**, 233–260.

Shah, R. K. & Focke, W. W. 1988 Plate heat exchangers and their design theory. In *Heat Transfer Equipment Design* (ed. R. K. Shah *et al.*), pp. 227–254. Hemisphere.

Shetty, L. & Cerro, R. L. 1993 Flow of a thin film over a periodic surface. *Intl J. Multiphase Flow* **l8**, 495–516.

Trifonov, Yu. Ya. 1998*a* Viscous liquid film flows over a periodic surface. *Intl J. Multiphase Flow* **24**, 1139–1161.

Trifonov, Yu. Ya. 1998*b* Viscous liquid film flows over a vertical corrugated surface and waves formation on the film free surface. In *3rd Intl Conf. on Multiphase Flow, Lyon, France.*

Vlachogiannis, M. & Bontozoglou, V. 2001 Observations of solitary wave dynamics of film flows. *J. Fluid Mech.* **435**, 191–215.

Wang, C.-Y. 1981 Liquid film flowing slowly down a wavy inclined. *AIChE J.* **27**, 207–212.

Webb, R. L. 1994 *Principles of Enhanced Heat Transfer*. Wiley.

Yih, C.-S. 1963 Stability of liquid flow down an inclined plane. *Phys. Fluids* **6**, 321–334.

Zhao, L. & Cerro R. L. 1992 Experimental characterization of viscous film flows over complex surfaces. *Intl J. Multiphase Flow* **18**, 495–516.